

# Zn<sub>1-x</sub>Sn<sub>x</sub>O<sub>y</sub> Buffer Layer Deposited by Chemical Bath Deposition for Low and Wide Bandgap Cu(In, Ga)Se<sub>2</sub> Solar Cells

Diego A. Garzón,\* Rafael Cerqueira, Cristiana F. Almeida Alves, Ana Margarida Moura, Jan Keller, Marika Edoff, Francis Leonard Deepak, and Sascha Sadewasser

Cu(In, Ga)Se<sub>2</sub> (CIGSe) solar cells with a tunable bandgap stand out as a promising technology for tandem applications. Addressing the environmental concerns associated with Cd-based buffers, this study investigates the suitability of zinc tin oxide (ZTO), deposited via chemical bath deposition (CBD), as a Cd-free alternative for both low-bandgap CIGSe and wide-bandgap (Ag, Cu)(In, Ga)Se<sub>2</sub> (ACIGSe) solar cells. Best ZTO-buffered devices exhibit competitive power conversion efficiencies (PCE) of 14% and 7% for low-bandgap and wide-bandgap absorbers, respectively. The optimal tin concentration for ZTO buffer layers vary, with 10% [Sn]/([Sn] + [Zn]) ratio (TTZ) identified as optimal for wide-gap ACIGSe and 20% TTZ for low-gap CIGSe. A performance decline beyond optimal tin concentrations could be linked to losses in open-circuit voltage. In summary, ZTO-based devices showcase promising photovoltaic performance, emphasizing ZTO's potential as a practical and nontoxic alternative, deposited by CBD, to traditional CdS for diverse CIGSe solar cell applications.

tunable bandgap (1.0–1.7 eV) and high absorption coefficient ( $>10^5 \text{ cm}^{-1}$ ),<sup>[2–4]</sup> making it a promising candidate for the production of clean and sustainable energy, with a laboratory power conversion efficiency (PCE) record of 23.6% (including Ag alloying).<sup>[5]</sup>

Tandem solar cells, involving stacking multiple absorbers with varying bandgaps, offer a pathway to enhance efficiency.<sup>[6]</sup> CIGSe, with its adjustable bandgap, is well-suited for integration as either the top or bottom cell in tandem devices. However, challenges arise, particularly in the performance of wide-bandgap CIGSe with a high [Ga]/([Ga] + [In]) ratio (GGI), which exhibits lower efficiency than anticipated, mostly related to losses in open-circuit voltage ( $V_{oc}$ ). As a consequence, CIGSe presents an optimum GGI in the

region of 0.25–0.30,<sup>[7,8]</sup> which has been assigned to several reasons including presence of Ga-rich compounds, as well as increase of bulk and interface recombination.<sup>[9,10]</sup> An increasing GGI also modifies the band alignment between absorber and the traditional CdS buffer layer.<sup>[11]</sup> Addressing this challenge, partly replacing the copper lattice sites with silver has shown improvement in the  $V_{oc}$ , related to better conduction band offset between high-Ga (Ag, Cu)(In, Ga)Se<sub>2</sub> (ACIGSe) and the buffer layer, with a maximum PCE of 15.1% for an absorber bandgap of 1.45 eV and a 16.3% when a RbF postdeposition treatment is applied ( $E_g = 1.44 \text{ eV}$ ).<sup>[12,13]</sup>

Traditional CdS, with its narrow bandgap ( $E_g = 2.4 \text{ eV}$ ), partly prevents high-energy photons to be absorbed by CIGSe.<sup>[14]</sup> Furthermore, for wide-bandgap applications it can increase the interface recombination due to its low electron affinity ( $\chi = 4.25 \text{ eV}$ ), related to a negative conductive band offset (CBO).<sup>[4,15]</sup> In this context, less-toxic wide-bandgap buffers such as Zn<sub>1-x</sub>Sn<sub>x</sub>O<sub>y</sub> (ZTO), In<sub>2</sub>S<sub>3</sub>, and Zn(O, S), among others have garnered attention.<sup>[16–19]</sup> ZTO, fabricated by atomic layer deposition (ALD), has outperformed CdS due to gains in short-circuit current ( $J_{sc}$ ) related to absorption of high-energy photons,<sup>[16,20]</sup> and gains in  $V_{oc}$  associated to better band alignment, especially for wide-bandgap CIGSe.<sup>[15]</sup>

Recently, we developed a solution-based method for depositing thick ZTO buffer layers by ammonia-based chemical bath deposition (CBD). This method allows for the tunability of the

## 1. Introduction

The urgency of addressing the ongoing environmental crisis has powered the exploration of renewable energy sources, with solar power emerging as a significant contributor, constituting 15% of global renewable energy.<sup>[1]</sup> Among photovoltaic technologies, Cu(In, Ga)Se<sub>2</sub> (CIGSe) stands out for its potential in flexible, semi-transparent, and tandem applications. This is attributed to its

D. A. Garzón, R. Cerqueira, C. F. Almeida Alves, A. M. Moura, F. L. Deepak, S. Sadewasser

International Iberian Nanotechnology Laboratory  
Avenida Mestre José Veiga s/n, 4715-330 Braga, Portugal  
E-mail: diego.garzon@inl.int

J. Keller, M. Edoff  
Ångström Solar Center  
Division of Solar Cell Technology  
Uppsala University  
75121 Uppsala, Sweden

The ORCID identification number(s) for the author(s) of this article can be found under <https://doi.org/10.1002/aesr.202500307>.

© 2025 The Author(s). Advanced Energy and Sustainability Research published by Wiley-VCH GmbH. This is an open access article under the terms of the Creative Commons Attribution License, which permits use, distribution and reproduction in any medium, provided the original work is properly cited.

DOI: 10.1002/aesr.202500307

ZTO bandgap (3.2–3.6 eV) by adjusting the  $[\text{Sn}]/([\text{Sn}] + [\text{Zn}])$  ratio (TTZ), providing a nontoxic alternative for wide-bandgap applications. This study reported an average PCE of  $9 \pm 2\%$  for an absorber of 1.16 eV and a ZTO buffer with nominal TTZ of 20% ( $\approx 10\%$ – $12\%$  in the film).<sup>[18]</sup> Moreover, CBD is recognized for its low-temperature ( $< 100^\circ\text{C}$ ) process, ensuring conformal growth in a reliable, cost-effective, and batch-scalable manner.<sup>[21]</sup>

Motivated by the promising outcomes of ZTO produced by ALD in both low and wide bandgap CIGSe, we fabricated high-efficient CIGSe solar cells with ZTO buffer layers using CBD. In this study, we investigate the current density–voltage (JV) characteristics of solar cell devices employing ZTO and CdS buffer layers, applied to both low-bandgap CIGSe (without silver alloying) and wide-bandgap ACIGSe, providing insights on the potential of ZTO as an effective buffer layer in CIGSe solar cells.

## 2. Results and Discussion

We fabricated low-bandgap CIGSe solar cells without a highly resistive layer depositing the conductive ZnO:Al (AZO) layers by sputtering directly on top of the buffer layers. Cross sectional scanning electron microscopy (SEM) images (Figure 1) show that for different TTZ in the bath deposition the buffer layer thickness varies. This variation indicates that the effect of Sn in the bath goes beyond modifying the ZTO bandgap or the ZTO/CIGSe interface, as previously reported.<sup>[18]</sup> For similar deposition time, the concentration of Sn in the bath also influences the thickness of the thin film. Nonetheless, no clear trend was observed and further investigation regarding the growth mechanism in the ZTO CBD process is required.

CIGSe solar cells with the ZTO buffer prepared from the 20% TTZ bath exhibit the best performance (Figure 2), yielding a mean PCE of  $(12 \pm 3)\%$  ( $J_{\text{sc,EQE}} = (38 \pm 2) \text{ mA cm}^{-2}$ ;  $\text{FF} = (60 \pm 9)\%$ ;  $V_{\text{oc}} = (520 \pm 34) \text{ mV}$ ), which is slightly lower than the CdS-based devices with a mean PCE of  $(13.7 \pm 0.5)\%$  ( $J_{\text{sc,EQE}} = (37 \pm 1) \text{ mA cm}^{-2}$ ;  $\text{FF} = (66.7 \pm 0.6)\%$ ;  $V_{\text{oc}} = (561 \pm 6) \text{ mV}$ ). It is worth noting that the ZTO layer obtained from this bath corresponds to the thickest buffer, with an average thickness of  $(0.21 \pm 0.08) \mu\text{m}$ . However, beyond 20% TTZ, a significant decline in performance was observed, caused by substantial losses in  $V_{\text{oc}}$  and FF.

To further investigate the ZTO structure and the low-bandgap CIGS/ZTO interface, Figure 3 shows the high-angle annular dark-field scanning transmission electron microscopy (HAADF-STEM) images and elemental maps for ZTO based solar cells prepared from baths with TTZ of 10%, 20%, and 30% (low magnification HAADF images can be seen in Figure S1, Supporting Information). The elemental maps of selenium are displayed to indicate the position of the ZTO/CIGSe interface. The apparent presence of Sn in the CIGSe layer is attributed to an overlap of the characteristic X-ray lines of In and Sn. In agreement with our previous report,<sup>[18]</sup> the 10% TTZ ZTO based devices exhibit some Sn-rich regions at the interface. Nonetheless, 20% TTZ ZTO solar cells display a more homogeneous distribution of Sn across the buffer layer, with an increase in concentration close to the interface with the absorber. At 30% TTZ, a thin Sn-rich layer is observed at the ZTO/CIGSe interface, suggesting formation of mainly a  $\text{SnO}_x$  interlayer, which could lead to a negative band offset with respect to CIGSe.<sup>[22]</sup> The latter is better observed on the elemental profiles across the CIGSe/ZTO/AZO interfaces (Figure S2, Supporting Information) and the elemental maps for oxygen (Figure S3, Supporting Information), which exhibit a higher concentration of Sn at the interface with CIGSe for all devices. It is worth mentioning that this result displays the complexity of the CBD process where the substrate plays an important role in the deposition of ZTO thin layers; for example, this thin  $\text{SnO}_x$  interlayer was not observed in our previous study.<sup>[18]</sup>

These Sn-rich regions are likely responsible for the open-circuit voltage drop (see Figure 2), caused by changes in the band alignment. The possible presence of  $\text{SnO}_x$  at the CIGS/ZTO interface would lead to a lower conduction band minimum (CBM) than ZnO, which could lead to a negative band offset with respect to CIGSe, as shown in the simulations in the supplementary information.<sup>[15,22]</sup> It is also worth noting that the thinner buffer layers obtained from the 10% and 30% TTZ baths exhibited different performance in terms of  $V_{\text{oc}}$  and FF, suggesting that thickness alone cannot account for the observed performance variations. SEM imaging revealed average thicknesses of  $(0.12 \pm 0.04)$  and  $(0.13 \pm 0.08) \mu\text{m}$  for 10% and 30% TTZ samples, respectively (see Figure 1).

Between 10% and 20% TTZ devices, the champion cells significantly differ due to an average difference in open-circuit voltage of 70 mV. Based on our previous report, the change from 10% to 20% TTZ in the bath corresponds to a change from

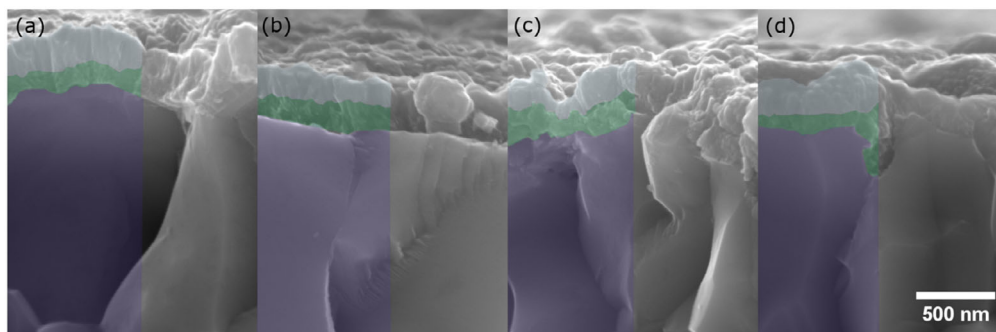


**Figure 1.** SEM cross-section images of low-bandgap devices with ZTO buffers of a) 10, b) 20, c) 25, and d) 30% TTZ. The left half of each image is artificially colored to guide the reader with colors corresponding to each layer: CIGSe (blue), ZTO (green), and AZO (gray).

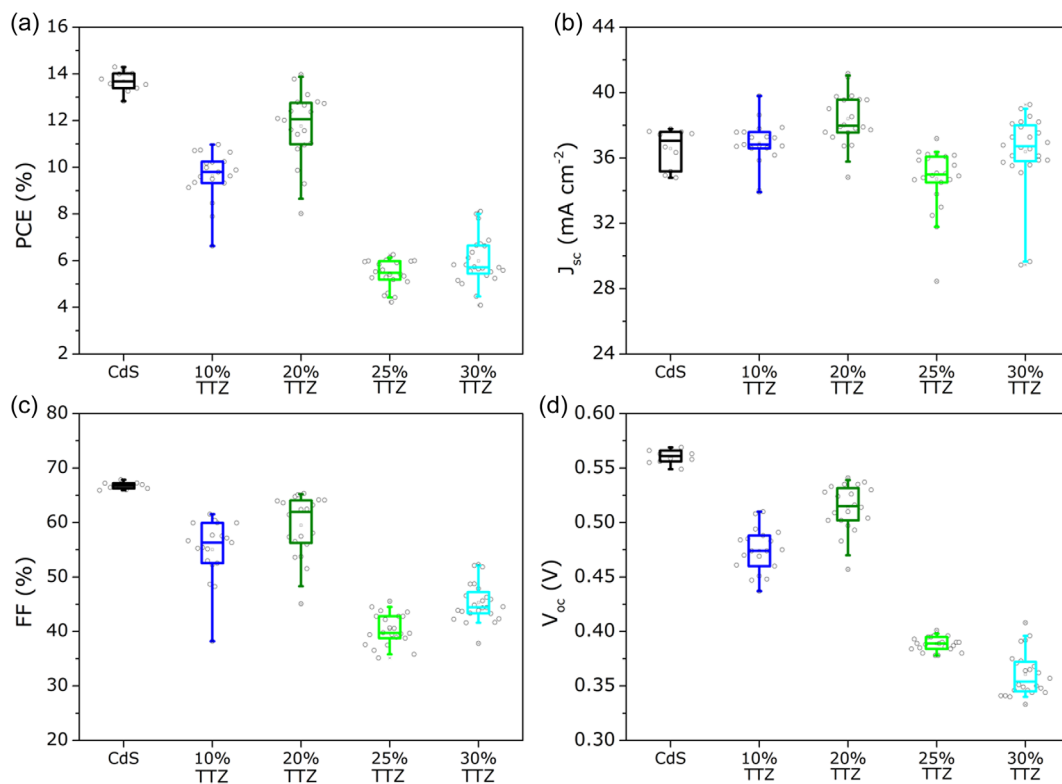


**Figure 2.** Solar cell parameters for CdS-based and ZTO-based devices with low bandgap CIGSe with different compositions of ZTO buffer layers: a) power conversion efficiency, b) short-circuit current density, c) fill factor, and d) open-circuit voltage.

7% to 12% TTZ in the film (Table S5, Supporting Information). Therefore, the Sn concentration in this range emerges as a critical parameter influencing the device's final performance.<sup>[18,23]</sup>

**Figure 4** shows the JV curves and external quantum efficiency (EQE) spectra for the low-bandgap CIGSe champion solar cells. All ZTO-based devices show improved carrier collection from high-energy photons due to the difference in bandgap between ZTO and CdS.<sup>[18]</sup> Furthermore, the EQE spectra for higher TTZ, 25% and 30%, show an initial onset at lower wavelengths, presumably related to a slightly wider bandgap for these layers.<sup>[18]</sup> The champion cells for 10, 25%, and 30% TTZ show a current loss in the near infrared region compared to CdS, presumably related to recombination at the ZTO/CIGS interface. In addition, the EQE spectra show that the bandgap of the absorbers is comparable for all samples with a value of 1.03 eV.

In terms of the champion solar cells, the solar cells with 20% TTZ ZTO buffer exhibit a performance similar to that of the reference cells with a CdS buffer, with a gain in  $J_{sc,EQE}$  of about  $1 \text{ mA cm}^{-2}$  and a loss in  $V_{oc}$  of 15 mV. This aligns with our latest reports, where a  $\approx 350 \text{ nm}$  ZTO buffer showed optimal performance.<sup>[18,19]</sup> However, thick buffer layers may generate performance losses due to the high resistivity of ZTO thin films. Nonetheless, our efforts on the deposition of thinner buffers resulted in inhomogeneous coverage. In addition, considering reports on ALD ZTO buffer layers with thicknesses as low as 20 nm,<sup>[20]</sup> further investigation into the impact of the ZTO buffer thickness is essential for a complete understanding of its effects on Cd-free CIGSe solar cells.

**Figure 5** shows SEM cross section images of the wide-bandgap ACIGSe/ZTO interfaces. For these devices the ZTO layers showed a similar morphology as AZO layers, which makes their distinction more difficult. Furthermore, ZTO layers seem to be thin but the imaging did not allow a clear measurement of the thickness. These changes in the ZTO buffer showcase the importance of the absorber (surface) in the CBD process, where different absorbers could promote or inhibit the growth of specific ZTO orientations.<sup>[24]</sup> However, the details of the ZTO growth are still unknown and further research is needed. One hypothesis relates to the process of nucleation, in which some crystal facets favor the growth while others inhibit it. Another possibility can be associated to a differential adsorption of metallic cations during the initial growth phase. Studies on Zn(S,O) buffer layers report also the effect of solution mixing on the final device performance related mainly with the deposition of particles/clusters,<sup>[25]</sup> so further research on the CBD process is necessary.

Regarding the solar cell parameters for wide-bandgap ACIGSe (**Figure 6**), we show several CdS references to account for differences in the absorber composition due to the geometry of the deposition system and the absence of substrate rotation creating compositional gradients in the absorber for the same deposition (**Table 1**). Regarding the differences within the CdS reference devices, an increase in performance variation was observed, which can be attributed to slight variations in the absorber layer. Nonetheless, the average PCE, FF, and  $V_{oc}$  of the CdS reference devices do not differ significantly at a 95% confidence level, whereas the  $J_{sc}$  shows a statistically significant difference

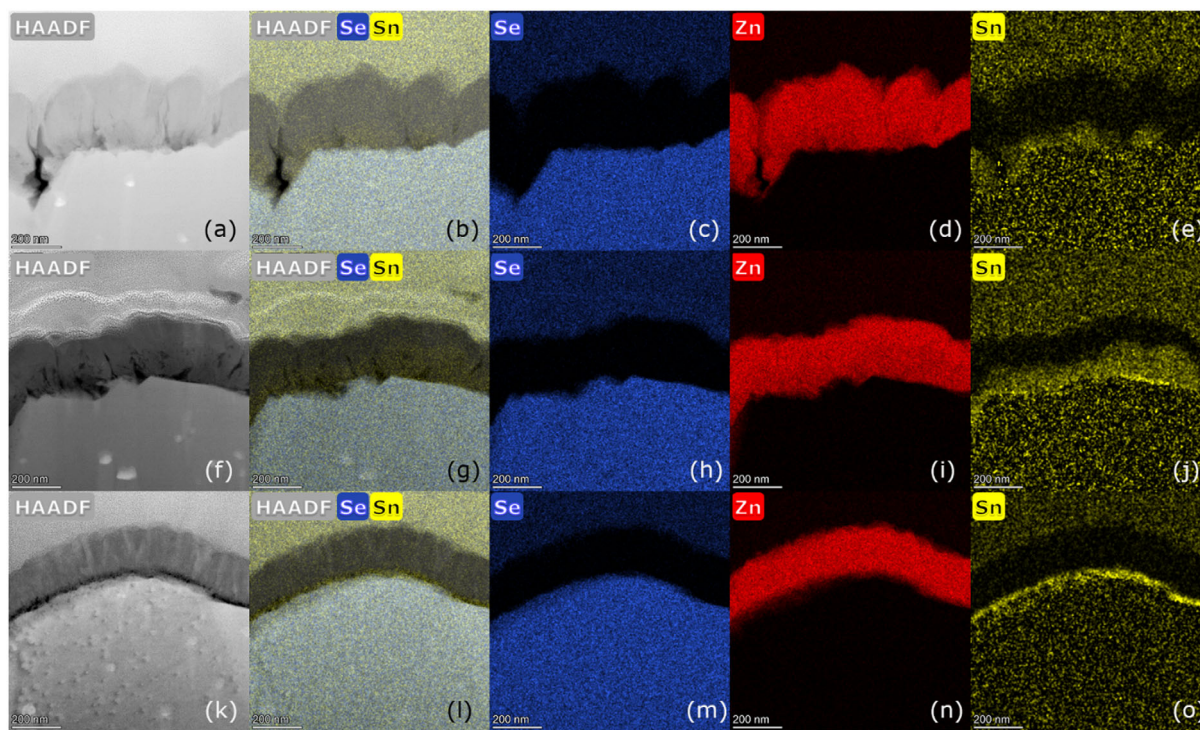


**Figure 3.** HAADF-STEM images of the ZTO with low-bandgap CIGSe solar cells: a) ZTO buffer layer with 10% TTZ, b–e) corresponding elemental maps from the area of the HAADF image for Sn + Se, Se (blue), Zn (red), and Sn (yellow) acquired by EDS. f) ZTO buffer layer with 20% TTZ and g–j) corresponding elemental maps from the area of the HAADF image for Sn + Se, Se, Zn, and Sn; k) ZTO buffer layer with 30% TTZ, and l–o) corresponding elemental maps.

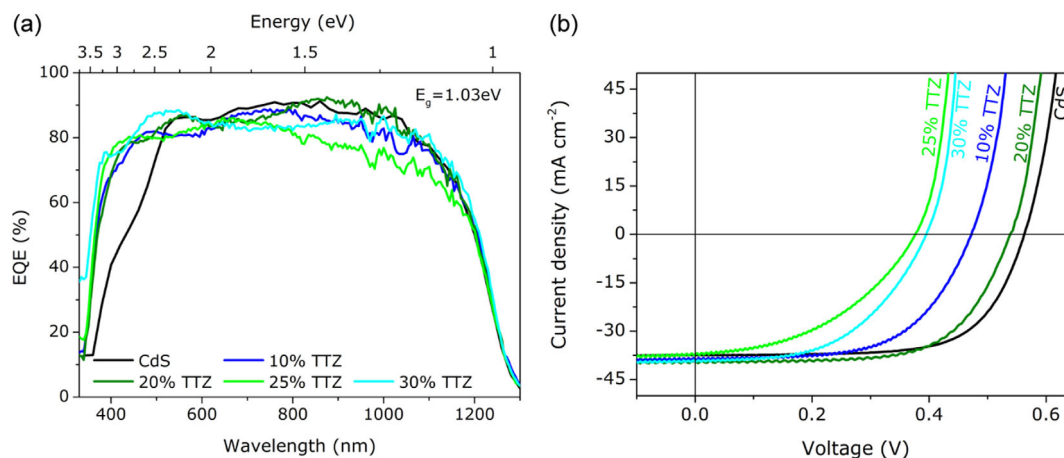


**Figure 4.** a) EQE spectra and b) JV curves under illumination for the best low-bandgap CIGSe solar cells with CdS and ZTO buffer layers.

between the references. Therefore, we conclude that it is valid to directly compare the overall solar cell performance across the different ZTO buffer layers, although the short-circuit current should not be directly compared. When comparing the ZTO-based devices with their respective CdS references, a gain in  $J_{sc}$  is observed for baths with a TTZ below 20%.

The 10% TTZ ZTO sample displays the best performance with a mean PCE of  $(6 \pm 1) \%$  ( $J_{sc, EQE} = (14 \pm 2) \text{ mA cm}^{-2}$ ; FF =  $(64 \pm 11) \%$ ;  $V_{oc} = (622 \pm 26) \text{ mV}$ ). In contrast, the best

CdS reference shows a mean PCE of  $(7 \pm 2) \%$  ( $J_{sc, EQE} = (12.9 \pm 0.6) \text{ mA cm}^{-2}$ ; FF =  $(63 \pm 14) \%$ ;  $V_{oc} = (785 \pm 98) \text{ mV}$ ). Also for the wide-bandgap absorber the fill factor is not significantly different compared to the CdS reference, which could indicate a less resistive front contact due to a thinner ZTO buffer layer. Likewise, we observed a similar trend with lower performance when increasing the TTZ, mostly related to losses in  $V_{oc}$ , similar to the case of low-bandgap CIGSe. Overall, the performance level of all wide-gap ACIGS cells is lower than previously reported,

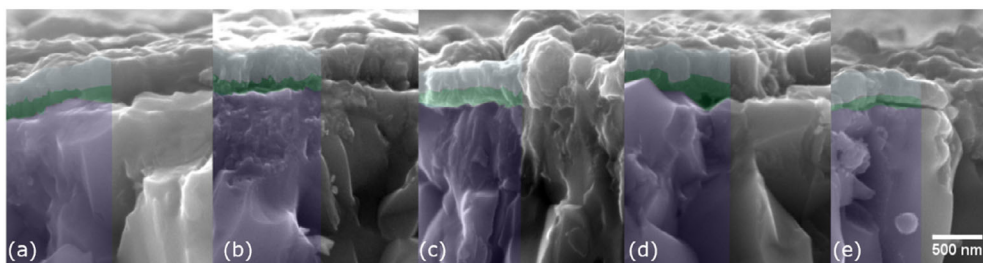


**Figure 5.** SEM cross-section images of ACIGSe wide-bandgap devices with ZTO buffers of a) 10, b) 13, c) 17, d) 20, and e) 30% TTZ. The left half of each image is artificially colored to guide the reader with colors corresponding to each layer: CIGSe (blue), ZTO (green), and AZO (gray).

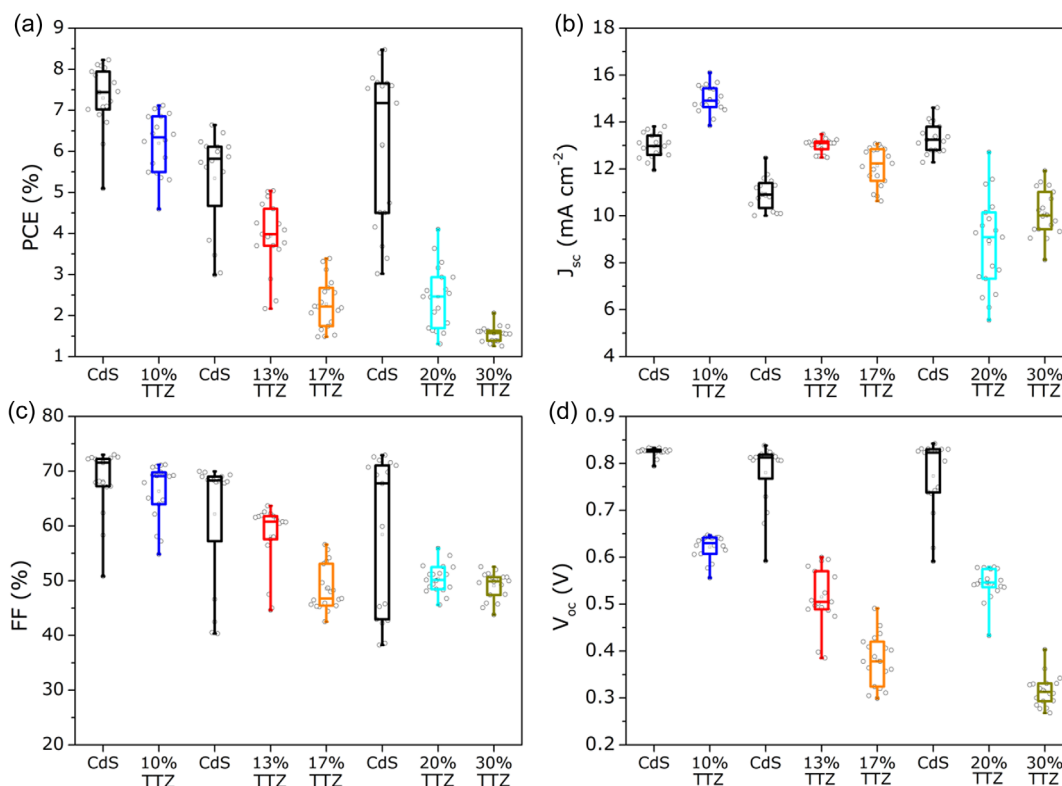


**Figure 6.** Solar cell parameters for CdS-based and ZTO-based devices with wide-bandgap ACIGSe with different compositions of ZTO buffer layers: a) power conversion efficiency, b) short-circuit current density, c) fill factor, and d) open-circuit voltage.

**Table 1.** Sample names of the investigated solar cells and corresponding integral atomic composition ratios as well as bandgap, estimated from EQE measurements.

Sample	Composition			E <sub>g</sub> [eV]
	I/III	GGI	AAC	
Low-bandgap CIGSe	0.91	0.24	0.0	1.03
Wide-bandgap ACIGSe	0.67–0.74	0.68–0.69	0.24–0.26	1.46

since the absorber composition was unintentionally very group-I poor ( $[I]/[III] \approx 0.7$ ), which might lead to the formation of detrimental ordered vacancy compounds at the surface and corresponding electron collection losses.<sup>[26]</sup>

It is known that silver alloying in wide-bandgap ACIGSe promotes better band alignment at the ACIGSe/buffer interface. Silver lowers the CBM, in contrast to increasing GGI, which raises the CBM, thereby allowing fine tuning of the absorber bands to match the buffer bands.<sup>[15]</sup> However, for the studied samples, absorber composition modifications were not significant. In this study, the ZTO buffer corresponding to the lowest bandgap ( $\approx 3.44$  eV)<sup>[18]</sup> and highest electron affinity ( $\approx 4.44$  eV)<sup>[23]</sup> outperformed the other ZTO buffers and displayed a PCE only  $\approx 1\%$ -point lower than the CdS reference. Assuming that the studied absorber behaves as the ones simulated by Keller et al.,<sup>[15]</sup> the studied absorber has a CBM close to 4.26 eV, which is very similar to the electron affinity of CdS ( $\chi = 4.25$  eV), thus the ACIGSe/CdS CBO should be close to zero.

Device simulations performed in SCAPS-1D show that a uniform ZTO buffer layer shows a CBO of  $-100$  meV, which corresponds to a cliff (Figure S4, Supporting Information). This cliff could be related to the loss in  $V_{oc}$ , which has an average difference of  $0.2$  V compared to the CdS reference. Further simulations varying the thickness and bandgap of a uniform ZTO buffer layer show a stronger dependence of the solar cell parameters on the thickness of the buffer layer (Figure S5, Supporting Information), with thinner buffers resulting in gains in efficiency and current, while thicker ZTO are related to better open-circuit voltage. The buffer layers change with the nominal TTZ in the deposition bath, which translates to a higher bandgap with lower thickness for high TTZ contents, thus these buffers rest within the trends observed in the simulated devices. Therefore, further characterization of the ZTO growth by CBD is required to optimize its structure, TTZ, and thickness, and thereby boost the final device performance, especially in terms of  $V_{oc}$ .

To further characterize the ACIGSe/ZTO interface, Figure 7 shows the HAADF-STEM imaging of the wide-bandgap devices (low magnification HAADF images can be seen in Figure S6, Supporting Information). Unlike SEM imaging, the STEM images allow a clear distinction between the buffer and AZO layers (Figure S7, Supporting Information). However, determining the exact thickness from these data is challenging because of the inhomogeneity commonly observed in ZTO prepared by CBD. The buffer thicknesses are below  $100$  nm, with thinner buffers as the TTZ increases. Contrary to the low-bandgap samples, the 10% TTZ device shows a homogenous distribution of Sn across the ZTO layer, while the 20% TTZ sample exhibits localized Sn-rich regions, as previously reported.<sup>[18]</sup>

Simulated devices with a double buffer layer composed of a thin  $\text{SnO}_2$  layer and a ZTO layer (details of the simulation in the supporting information, Table S5, Supporting Information) show a harmful effect of the thin  $\text{SnO}_2$  layer on the device performance on both low (Figure S8, Supporting Information) and wide (Figure S9, Supporting Information) bandgap CIGSe, mainly impacting the  $V_{oc}$ . Furthermore, the simulated devices with thin  $\text{SnO}_2$  layer show poorer performance with the increase of the ZTO bandgap, due to pronounced cliffs ( $-130$  and  $-290$  meV for low and wide bandgap devices, respectively) in the conduction band alignment. As observed above, the thickness of the ZTO layer decreases for higher TTZ. According to literature, thinner ZTO buffer layers prepared by ALD have been reported to yield higher  $V_{oc}$  values compared to their thicker counterparts,<sup>[20]</sup> yet this trend does not hold for the CBD-grown ZTO layers or the simulated devices. Our data indicate that this difference is since higher concentrations in Sn not only result in thinner layers but also in accumulation of Sn-rich regions at the interface with the absorber. Although thinner devices work better, according to literature and simulations, the accumulation of Sn has a stronger impact on the performance of the device, affecting both its  $V_{oc}$  and  $J_{sc}$ .

Furthermore, for the 30% TTZ sample the elemental maps show that Sn mainly accumulates at the interface with the absorber, similar to the case of low-bandgap CIGSe, but there is not a clear continuity within the Sn-rich regions. The latter can be also observed in the elemental profiles across the ACIGSe/ZTO/AZO interfaces (Figure S10, Supporting Information), where a peak in Sn content is only observed for the 30% TTZ sample. Likewise, these Sn-rich regions, which

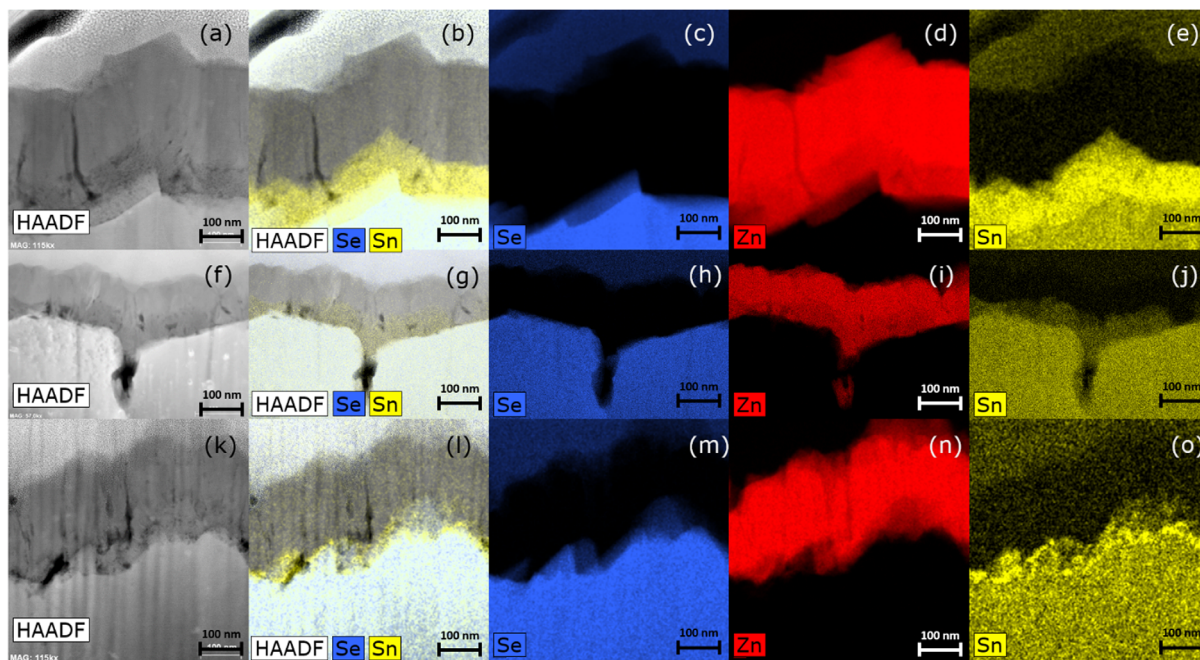


**Figure 7.** HAADF-STEM images of the ZTO with wide-bandgap CIGSe solar cells. For each sample, the HAADF image together with the corresponding elemental maps for Sn + Se, Se (blue), Zn (red), and Sn (yellow) acquired by EDS are shown. The images correspond to devices with a ZTO buffer layer with TTZ of a–e) 10%, f–j) 20%, and k–o) 30%.

mainly are composed of  $\text{SnO}_x$ , are detrimental for the final device performance.

**Figure 8** shows the JV curves and EQE spectra for the champion cells for the wide-bandgap ACIGSe absorber. The CdS-based reference device outperforms all ZTO-based devices mainly due to a  $V_{oc}$  of 0.8 V; the 10% TTZ ZTO based device achieves 0.64 V. We attribute this loss in open-circuit voltage to both the thickness and the CBO cliff at the ACIGSe/ZTO interface, based on the simulations performed. This contrasts with the reported observation of a “spike” configuration and a gain in  $V_{oc}$  for thin ALD-ZTO.<sup>[15]</sup> Furthermore, the EQE spectrum for the 10% TTZ ZTO-based device shows higher photon absorption for all wavelengths compared to other studied buffers. EQE spectra also show no parasitic absorption in the blue region due to the substitution of CdS, together with a slightly oscillatory behavior, previously observed and attributed to high reflectance.<sup>[15,18]</sup>

Assuming a reproducible process, the films grown in the 10% TTZ bath are expected to have a Sn content close to 7% (Table S6, Supporting Information), different from the optimal value of  $\approx 20\%$  found for ALD-ZTO buffer layers for wide-bandgap ACIGSe.<sup>[15,16]</sup> Nevertheless, by considering the STEM imaging, a higher TTZ content gives rise to the formation of Sn-rich regions that are detrimental to the final device performance. This indicates that an ideal ZTO buffer layer for wide-bandgap CIGSe must have a higher Sn content without the presence of Sn-rich regions or inhomogeneities at the interface with the absorber.

For both absorbers studied, ZTO buffers prepared with a 30% TTZ present low performance due to losses in both FF and  $V_{oc}$ , mainly related with the presence of a thin Sn-rich layer at the CIGSe/ZTO interface that creates a cliff arrangement, resulting in losses in FF, in agreement with the simulations shown in the supplementary information. Furthermore, based on the EDS the best performance corresponds to the most homogenous buffer layer in terms of Sn content, but it is interesting to notice that the substrate plays a role in the distribution of Sn within the ZTO layer, being 10% TTZ for ACIGSe and 20% TTZ for CIGSe, even though the buffer deposition baths were similar for both substrates.

### 3. Conclusion

In this study, ZTO buffer layers were successfully deposited by CBD on both low-bandgap CIGSe and wide-bandgap ACIGSe absorbers, achieving competitive PCE of 14% and 7%, respectively. The optimization process revealed distinct optimal nominal tin concentrations in the bath deposition for the two absorbers, with 10% TTZ ZTO identified as optimal for the wide-bandgap samples, and 20% TTZ ZTO for the low-bandgap material. A pronounced decline in performance was observed for both materials when higher Sn content buffer layers were used, mainly due to losses in open-circuit voltage. These open circuit voltage losses presumably stem from poor band alignment, providing a plausible explanation for the results obtained in the low-bandgap CIGSe sample. Further characterization of the CIGSe/ZTO interface showed that the best performance devices for both low and high bandgap absorbers present a more homogenous buffer layer and in both cases the presence of Sn-rich regions (presumably  $\text{SnO}_x$ ), locally creating an unfavorable negative conduction band offset, are detrimental to the final device performance. In addition, the results showcase the importance of the substrate in the CBD of ZTO, as similar bath conditions gave result to different thin films in terms of morphology and Sn composition.

Overall, ZTO-based devices demonstrated promising photovoltaic performance with PCE values of  $(12 \pm 3) \%$  for low-bandgap CIGSe and  $(6 \pm 1) \%$  for wide-bandgap ACIGSe. For both types of absorbers, ZTO-based devices show a performance that is not significantly different compared to CdS-based references, even though CdS champion reference cells surpass ZTO champion cells. Further optimization in the control of the Sn distribution within the buffer layer is required. These results emphasize the viability of ZTO, deposited by CBD, as a practical and non-toxic alternative to CdS for both wide- and low-bandgap CIGSe solar cells.

### 4. Experimental Section

**Device Characterization:** The absorber layers of the devices were deposited using a three-stage coevaporation process, with a maximum

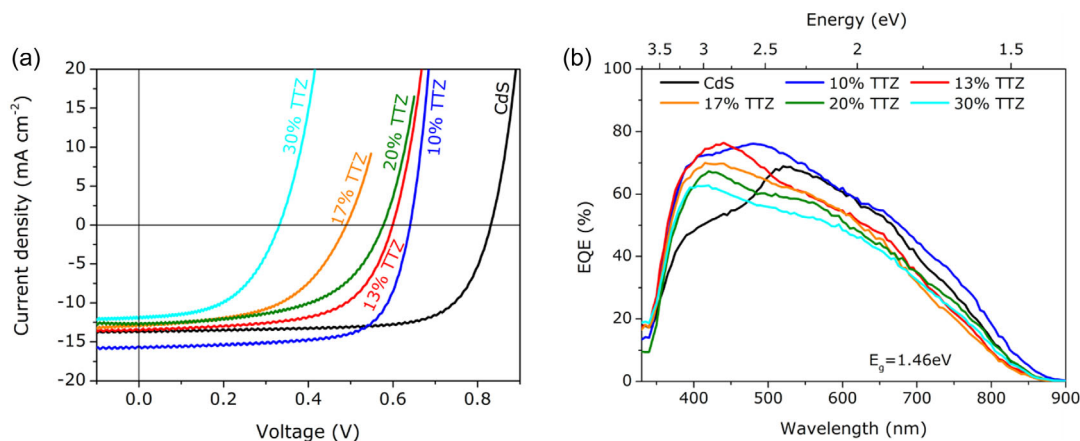


**Figure 8.** a) JV curves under illumination and b) EQE spectra for the best wide-bandgap ACIGSe solar cells with CdS and ZTO buffer layers.

temperature of 550 °C; further details can be found elsewhere.<sup>[27]</sup> CBD was used for both the CdS and ZTO buffer layers. After absorber deposition a protective CdS layer was deposited on top of the absorber by CBD. The deposition bath was prepared by the consecutive addition of NH<sub>4</sub>OH (4.4% v/v), cadmium acetate (17 mM), and thiourea (0.35 M). The depositions were carried out at 60 °C for 8.5 min. Prior to the ZTO deposition, an HCl-etching was done for 90 s with HCl ≈9% to remove the protective CdS layer. The ZTO deposition bath was prepared by the consecutive addition of aliquots of ZnSO<sub>4</sub>, NH<sub>4</sub>OH, ethanolamine, and SnCl<sub>2</sub> (prepared in HCl 1.7 M) stock solutions to obtain a final concentration of 75 mM of cations ([Zn<sup>2+</sup>] + [Sn<sup>2+</sup>]), 0.2 M NH<sub>4</sub>OH, and 1.6 M ethanolamine. The depositions were carried out at 92 °C for 30 min with a variation of TTZ in the range of 10%–30%.<sup>[18]</sup> Then, the ZnO:Al front contact (≈0.21 μm) was deposited directly on top of the buffer by RF sputtering. Finally the solar cells were mechanically scribed with an area of 0.05 cm<sup>2</sup> and measured directly on the front contact. Table 1 shows the composition of the absorbers used in this study, based on X-ray fluorescence (XRF) analysis.

Completed solar cells were characterized by EQE measurements and by JV analysis at  $T = 25$  °C under illumination by an ELH lamp in home-built setups. Illumination intensity was adjusted to the short-circuit current density as extracted from the EQE spectra ( $J_{SC, EQE}$ ). The bandgap of the absorbers was estimated as the x-intercept of a linear regression following a linear fit, where  $(\ln(1-EQE) \times E)^2 \propto E - E_g$ .

Cross-section micrographs of the finished devices were obtained by SEM in an FEI Quanta 50 FEG SEM. Furthermore, these devices were also analyzed by STEM and energy dispersive spectroscopy (EDS). First, cross-sectional samples were prepared using a FEI Helios NanoLab 450S focused ion beam (FIB) to have electron-transparent lamellae (thickness < 100 nm) for subsequent STEM/EDS analysis. The FIB operates with a gallium (Ga) liquid metal ion source, which is the reason why we deliberately abstain from quantifying the Ga content in the analyzed samples. Second, HAADF-STEM imaging was performed with a probe-corrected FEI Titan G2 80–200 keV ChemiSTEM (wide-bandgap ACIGSe devices), and double-corrected FEI Titan G3 Cubed Themis 60–300 keV (low-bandgap CIGSe devices), both operated at 200 keV.

While using the double-corrected Titan Themis, the images, captured at a resolution of 2048 × 2048 pixels, were acquired using a 21 mrad convergence angle and a pixel dwell time of 8 μs. For elemental mapping, EDS analysis was performed using a Super-X EDS detector. Iterative maps of 2048 × 2048 pixels were collected with a pixel dwell time of 5 μs at 200 keV, under beam current ranging from 150 to 250 pA, with a total acquisition time of 15 min. The STEM-EDS data was acquired and processed using Velox software from Thermo Fisher Scientific. Regarding the probe-corrected ChemiSTEM, the images of 2048 × 2048 pixels were recorded using a convergence angle of 21 mrad with pixel dwell time set to 8 μs. EDS-mapping was performed with the same instrument using a Super-X EDS detector. Iterative maps of 1024 × 1024 pixels were recorded with a dwell time per pixel of 13 μs at 200 keV, and collection times of at least 15 min. The software Esprit from Bruker was used for acquiring and processing the STEM-EDS data.

## Supporting Information

Supporting Information is available from the Wiley Online Library or from the author.

## Acknowledgements

The authors acknowledge funding by the European Union under the European Innovation Council Pathfinder Open scheme grant no. 101046909: REMAP, Reusable Mask Patterning. The authors acknowledge support by the project “Designing superior CIGSe solar cells through understanding and controlling growth (Design-Solar)” (PTDC/CTM-CTM/2241/2021), funded by FCT - Fundação para a Ciência e a Tecnologia. This work was financially also supported by the European

Union program HORIZON (Call: HORIZON-CL5-2021-D3-02), Project ID: 101075626 (SITA). Views and opinions expressed are however those of the authors only and do not necessarily reflect those of the European Union or of the European Innovation Council. Neither the European Union nor the granting authority can be held responsible for them. D.A.G. acknowledges the support by FCT - Fundação para a Ciência e Tecnologia, I.P. with the project reference 2023.00258.BD and DOI identifier <https://doi.org/10.54499/2023.00258.BD>.

## Conflict of Interest

The authors declare no conflict of interest.

## Data Availability Statement

The data that support the findings of this study are available from the corresponding author upon reasonable request.

## Keywords

(Ag, Cu)(In, Ga)Se<sub>2</sub>, buffer layers, chemical bath deposition, Cu(In, Ga)Se<sub>2</sub>, thin film solar cells, zinc tin oxide

Received: July 18, 2025  
Revised: December 12, 2025  
Published online:

- [1] H. Ritchie, M. Roser, P. Rosado, *Our World in Data* **2022**.
- [2] E. Mirabi, F. Akrami Abarghuie, R. Arazi, *Clean Energy* **2021**, *5*, 505.
- [3] A. Ashok, J. S. Narro-Rios, O. Nwakanma, G. Regmi, S. Velumani, F. A. Pulgarin-Agudelo, in *2018 15th International Conference on Electrical Engineering, Computing Science and Automatic Control (CCE)* **2018**, *1*.
- [4] S. Wei, A. Zunger, *J. Appl. Phys.* **1995**, *78*, 3846.
- [5] J. Keller, K. Kiselman, O. Donzel-Gargand, N. M. Martin, M. Babucci, O. Lundberg, E. Wallin, L. Stolt, M. Edoff, *Nat. Energy* **2024**, *9*, 1.
- [6] O. M. Saif, A. H. Zekry, M. Abouelatta, A. Shaker, *Silicon* **2023**, *15*, 6329.
- [7] B. Huang, S. Chen, H.-X. Deng, L.-W. Wang, M. A. Contreras, R. Noufi, S.-H. Wei, *IEEE J. Photovoltaics* **2014**, *4*, 477.
- [8] M. A. Contreras, L. M. Mansfield, B. Egaas, J. Li, M. Romero, R. Noufi, E. Rudiger-Voigt, W. Mannstadt, *Prog. Photovolt.: Res. Appl.* **2012**, *20*, 843.
- [9] M. Raghuvanshi, E. Cadel, P. Pareige, S. Duguay, F. Couzinie-Devy, L. Arzel, N. Barreau, *Appl. Phys. Lett.* **2014**, *105*, 013902.
- [10] M. Raghuvanshi, PhD Thesis, University of Rouen **2015**.
- [11] J. V. Li, S. Grover, M. A. Contreras, K. Ramanathan, D. Kuciauskas, R. Noufi, *Sol. Energy Mater. Sol. Cells* **2014**, *124*, 143.
- [12] J. Keller, L. Stolt, T. Törndahl, M. Edoff, *Solar RRL* **2023**, *7*, 2300208.
- [13] J. Keller, H. Aboufadel, L. Stolt, O. Donzel-Gargand, M. Edoff, *Solar RRL* **2022**, *6*, 2200044.
- [14] J. M. Doña, J. Herrero, *J. Electrochem. Soc.* **1997**, *144*, 4091.
- [15] J. Keller, K. V. Sopiha, O. Stolt, L. Stolt, C. Persson, J. J. S. Scragg, T. Törndahl, M. Edoff, *Prog. Photovolt.: Res. Appl.* **2020**, *28*, 237.
- [16] J. Lindahl, PhD Thesis, Acta Universitatis Upsaliensis **2015**.
- [17] G. Regmi, A. Ashok, P. Chawla, P. Semalti, S. Velumani, S. N. Sharma, H. Castaneda, *J. Mater. Sci.: Mater. Electron* **2020**, *31*, 7286.
- [18] D. A. Garzón, C. Rossi, I. Khatri, F. Soggia, I. Çaha, F. L. Deepak, D. Colombara, S. Sadewasser, *Solar RRL* **2023**, *7*, 2300173.

- [19] D. A. Garzon, M. Alves, P. Sousa, J. Fonseca, D. Brito, J. Carneiro, S. Sadewasser, *J. Phys. Energy* **2025**, *7*, 035011.
- [20] J. Lindahl, J. T. Wätjen, A. Hultqvist, T. Ericson, M. Edoff, T. Törndahl, *Prog. Photovolt.: Res. Appl.* **2013**, *21*, 1588.
- [21] Y. Hashimoto, N. Kohara, T. Negami, N. Nishitani, T. Wada, *Sol. Energy Mater. Sol. Cells* **1998**, *50*, 71.
- [22] M. Kapilashrami, C. X. Kronawitter, T. Törndahl, J. Lindahl, A. Hultqvist, W.-C. Wang, C.-L. Chang, S. S. Mao, J. Guo, *Phys. Chem. Chem. Phys.* **2012**, *14*, 10154.
- [23] J. Lindahl, J. Keller, O. Donzel-Gargand, P. Szaniawski, M. Edoff, T. Törndahl, *Sol. Energy Mater. Sol. Cells* **2016**, *144*, 684.
- [24] F. Gashaw Hone, T. Abza, *Int. J. Thin Film Sci. Technol.* **2019**, *8*, 43.
- [25] J. Li, L. Huang, J. Hou, X. Wu, J. Niu, G. Chen, J. Gong, Y. Kong, X. Xiao, *Nano Energy* **2019**, *58*, 427.
- [26] J. Keller, N. Martin, O. Donzel-Gargand, K. Kiselman, U. Zimmermann, L. Stolt, C. Platzer-Björkman, M. Edoff, *Solar RRL* **2024**, *8*, 2301018.
- [27] J. Keller, P. Pearson, N. Shariati Nilsson, O. Stolt, L. Stolt, M. Edoff, *Solar RRL* **2021**, *5*, 2100403.